Microscopy and Microanalysis (2021), **27**, 1102–1112
doi:10.1017/S1431927621012538

Microscopy AND Microanalysis

Original Article

Automated Crystal Orientation Mapping by Precession Electron Diffraction-Assisted Four-Dimensional Scanning Transmission Electron Microscopy Using a Scintillator-Based CMOS Detector

Jiwon Jeong*, Niels Cautaerts, Gerhard Dehm and Christian H. Liebscher
Max-Planck Institut für Eisenforschung GmbH, Düsseldorf 40237, Germany

Abstract

The recent development of electron-sensitive and pixelated detectors has attracted the use of four-dimensional scanning transmission electron microscopy (4D-STEM). Here, we present a precession electron diffraction-assisted 4D-STEM technique for automated orientation mapping using diffraction spot patterns directly captured by an in-column scintillator-based complementary metal-oxide-semiconductor (CMOS) detector. We compare the results to a conventional approach, which utilizes a fluorescent screen filmed by an external charge charge-coupled device camera. The high-dynamic range and signal-to-noise characteristics of the detector greatly improve the image quality of the diffraction patterns, especially the visibility of diffraction spots at high scattering angles. In the orientation maps reconstructed via the template matching process, the CMOS data yield a significant reduction of false indexing and higher reliability compared to the conventional approach. The angular resolution of misorientation measurement could also be improved by masking reflections close to the direct beam. This is because the orientation sensitive, weak, and small diffraction spots at high scattering angles are more significant. The results show that fine details, such as nanograins, nanotwins, and sub-grain boundaries, can be resolved with a sub-degree angular resolution which is comparable to orientation mapping using Kikuchi diffraction patterns.

Key words: four-dimensional scanning electron microscopy (4D-STEM), orientation mapping, precession electron diffraction (PED), transmission electron microscopy (TEM)

(Received 7 March 2021; revised 10 July 2021; accepted 25 July 2021)

Introduction

The size and orientation of grains in nanocrystalline materials are directly related to material properties (Meyers et al., 2006). Therefore, the quantitative measurement of local crystallographic orientations is required to understand the structure–property relationship at nanometer scales. For this purpose, several transmission electron microscopy (TEM)-based methods (Schwarzer, 1997) have been developed, such as dark-field conical scanning (Li & Williams, 2003; Dingley, 2006; Wu & Zaefferer, 2009), convergent beam electron diffraction (Fundenberger et al., 2003), and nanobeam diffraction (NBD) in scanning transmission electron microscopy (STEM) (Ganesh et al., 2010). Scanning precession electron diffraction (SPED) is also widely used in TEM because the acquisition of diffraction patterns and orientation indexing of each pattern can be carried out automatically which is suitable for automated crystal orientation mapping (Rauch et al., 2008, 2010; Portillo et al., 2010; Viladot et al., 2013; Cooper et al., 2015). Diffraction patterns of individual crystallites are acquired by scanning a focused electron beam in a two-dimensional (2D) array on the sample and synchronized 2D diffraction patterns are recorded at each probe position, referred to as 4D-STEM (Ophus, 2019).

In SPED, the 4D-STEM method is extended by the precession of the ∼1 nm-sized incident beam at a constant angle on a conical surface around the optic axis. By recording diffraction patterns with the incident electron beam in precession, the diffraction spot intensities are integrated with an angular range across different diffraction conditions. As a result, quasi-kinematical conditions are achieved by suppressing dynamical scattering effects and a wider range of reflections is excited, which greatly improves the quantitative interpretability of diffraction patterns (Vincent & Midgley, 1994; Own et al., 2006; Oleynikov et al., 2007; Portillo et al., 2010). An orientation map is reconstructed by indexing each diffraction pattern in the 4D-STEM dataset using a template matching algorithm (Rauch & Dupuy, 2005; Rauch et al., 2010). SPED enables phase identification and local crystallographic orientation determination of nanostructured or nanocrystalline materials with a high spatial resolution.

However, orientation indexing is often difficult when the acquired diffraction pattern contains all reflections from superimposed grains along the sample thickness (Kobler & Kübel, 2017; Rauch & Véron, 2019). In addition, detailed features such as sub-grain boundaries are difficult to resolve with SPED because of the limited angular resolution (∼1°) of the technique (Zaefferer, 2011;

*Corresponding author: Jiwon Jeong, E-mail: j.jeong@mpie.de

Cite this article: Jeong J, Cautaerts N, Dehm G, Liebscher CH (2021) Automated Crystal Orientation Mapping by Precession Electron Diffraction-Assisted Four-Dimensional Scanning Transmission Electron Microscopy Using a Scintillator-Based CMOS Detector. *Microsc Microanal* 27, 1102–1112. doi:10.1017/S1431927621012538

© The Author(s), 2021. Published by Cambridge University Press on behalf of the Microscopy Society of America. This is an Open Access article, distributed under the terms of the Creative Commons Attribution licence (http://creativecommons.org/licenses/by/4.0/), which permits unrestricted re-use, distribution, and reproduction in any medium, provided the original work is properly cited.

CrossMark

Morawiec et al., 2014). In scanning electron microscopy (SEM), transmission Kikuchi diffraction (TKD) has been used as an alternative method for the characterization of nanomaterials because it has the required spatial resolution and high angular resolution (Trimby et al., 2014; Sneddon et al., 2016; Liu et al., 2019; Ernould et al., 2020; Sugar et al., 2020; Jeong et al., 2021).

The conventional SPED system cannot utilize the orientation sensitive, weak, and small diffraction spots at high scattering angles due to the difficulty of capturing those reflections. In conventional SPED configurations, an external charge-coupled device (CCD) camera is used to capture diffraction patterns from a fluorescent screen during nanobeam scanning (Moeck et al., 2011). When the diffracted electrons collide with a fluorescent screen, a phosphor on the fluorescent screen is excited. This produces emitted visible light proportional to the electron intensities on the fluorescent screen. The external CCD camera captures this light as images with an off-axis geometry, which are passed through additional postprocessing steps, such as distortion and inclination corrections (Moeck et al., 2011; Eggeman et al., 2015; Yao et al., 2016). Although the CCD camera has a high frame rate (∼180 frames/s) and high sensitivity for fast mapping (Moeck et al., 2011), acquired patterns contain afterimages from the last several positions of the probe because the fluorescent screen continues to emit light ∼100 ms after a diffraction spot has disappeared (Shionoya & Yen, 1998). Due to the various electron to light and light to electron conversion steps in current data acquisition systems, the signal-to-noise ratio for this technique is suboptimal. Hence, this conventional SPED configuration suffers from limitations that introduce scanning artifacts, obscure the detection of weak reflections and strongly restrict the angular resolution of this spot-based technique in the TEM.

Although there is a detrimental effect due to the suboptimal configuration of the conventional system, in-built detector configurations consisting of a CCD sensor with a phosphor and fiber-optic coupling were not widely used due to limited dynamic range and slow-scan speed in the past (Fan & Ellisman, 1993). The phosphor (and fiber-optic), which converts the signal from a high-energy incident electron into a pulse of light photons, was an essential component because the CCD sensor is easily damaged by direct illumination of the focused electron beam. In TEM, recent advances have focused on the development of direct electron detectors in which incident electrons directly create electron–hole pairs and then read out in a semiconductor (Clough et al., 2014; McMullan et al., 2016). High dynamic range, high electron sensitivity, and readout speed of those detectors have propelled their application in numerous 4D-STEM applications (Ophus, 2019). One type of direct electron detectors is a hybrid pixel array detector (PAD) which can be used for capturing high-intensity reflections with a high dynamic range (Yang et al., 2015; Mir et al., 2017*a*; Nord et al., 2020). A diffraction pattern is recorded as an image with a low number of pixels (Normally 256×256 pixels) with a large pixel pitch in favor of high electron sensitivity. Recently, MacLaren et al. showed an improvement in phase and orientation indexing reliability using diffraction patterns acquired by a hybrid PAD (MacLaren et al., 2020). Another type of detector is complementary metal-oxide-semiconductor (CMOS) based on monolithic active pixel sensors (APS). This CMOS with APS allows bigger arrays (16, 24, or 64 megapixels), faster readout, reduced noise, and reduced sensitivity to radiation damage compared with CCD (Ghadimi et al., 2011; Bammes et al., 2012; Contarato et al., 2012). However, this type of detector has limited applicability for capturing NBD patterns including the high intensity transmitted beam because the detector can be damaged by high electron dose due to the very thin electron-sensitive volume. This drawback can be overcome by using a scintillator-coupled CMOS detector. Although electron sensitivity can be slightly degraded due to the configuration of indirect electron detection, the dynamic range and capacity of high electron dose can be adapted by optimizing the scintillator (Rodriguez & Gonen, 2016). However, orientation mapping using a scintillator-coupled CMOS detector has not been thoroughly investigated or discussed yet.

In this study, we demonstrate orientation mapping with precession electron diffraction (PED)-assisted 4D-STEM using a scintillator-coupled CMOS detector in TEM. In each nanobeam probe position, a high-quality diffraction pattern is acquired with a simultaneous precession of the electron nanobeam. The scintillator was found to be robust during measurement in a TEM operating at 200 kV. Considering the widespread use of the conventional SPED system in nanoscale orientation analysis, we first compared two systems (i.e. the conventional system and a scintillator coupled CMOS detector) by collecting 4D-STEM datasets in the same area of a sample. The data are compared in terms of the quality of the diffraction patterns and orientation maps. The following section focuses on the CMOS system with the optimization of the template matching process to improve the angular resolution of diffraction spot patterns.

Experimental Procedures

TEM Sample Preparation

For quantitative measurement of diffraction pattern images, a thin lamella of single-crystal Si was prepared in a Scios 2 focused ion beam (FIB, ThermoFisher). The acceleration voltage of the Ga^+ ion beam during FIB milling was 30 kV. To minimize the surface damage layers, a final low-energy cleaning step was performed at 0.5 kV.

For orientation mapping, a thin foil of nanocrystalline Cu–Ag alloy with a thickness of 5 μm was used (Oellers et al., 2020). A disc with a diameter of 3 mm was cut out from the foil using a disc puncher and glued to a Cu single hole grid. For perforation, Ar^+ ion milling was performed at 2.5 kV using a PIPS II system (Gatan). Low-energy milling was followed at 0.5 kV to minimize the surface damage and to extend the electron transparent area.

PED-Assisted 4D-STEM Data Acquisition

PED was performed in a JEM-2200FS TEM (JEOL) operating at 200 kV and equipped with ASTAR (Nanomegas). The microscope was operated in NBD mode with the smallest spot size and a condenser aperture size of 10 μm. The probe size was measured as ∼ 1 nm in diameter with a convergence angle of 2 mrad. A precession frequency of 100 Hz and a precession angle of 0.5° were applied during the nanobeam scanning.

The overall procedure of the orientation mapping using the conventional configuration and the in-column CMOS system are summarized in Figure 1, respectively. To compare the data quality between the conventional and CMOS camera systems, PED patterns and datasets were acquired in the same region on the same specimen. The first dataset was acquired using the conventional off-axis system filming the fluorescent screen with a Stingray CCD camera (NanoMegas) (labeled as "Conventional" in Fig. 1). This setup is referred to as the conventional

https://doi.org/10.1017/S1431927621012538 Published online by Cambridge University Press

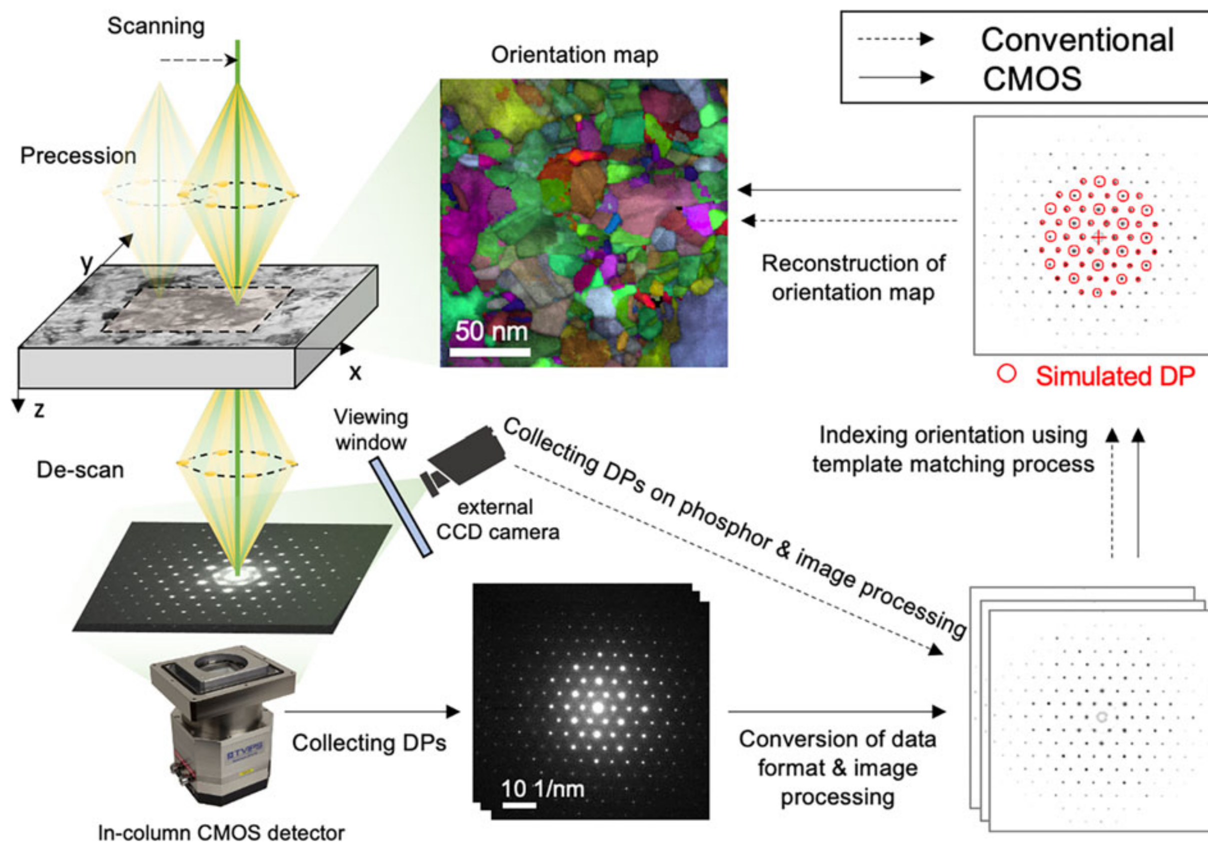

Fig. 1. Overview of PED orientation mapping analysis using conventional and CMOS camera systems used in the present study.

configuration in the remainder of the paper. Each acquired pattern has 144 × 144 pixels with an 8-bit depth. The scan size was 150 × 75 pixels with a step size of 2 nm, yielding a scanning area of 300 × 150 nm^2. The second dataset was recorded using an on-axis TemCam-XF416 pixelated CMOS detector (TVIPS) (labeled as "CMOS" in Fig. 1). The Universal scan generator (TVIPS) was used for synchronizing the scanning with the acquisition of diffraction patterns. The step size was ∼2.7 nm for the same scanning area of 300 × 150 nm^2. The diffraction patterns had a pixel size of 2k × 2k (2× hardware binning of the full 4k detector area) with 16-bit depth. The exposure time for the acquisition of each diffraction pattern was chosen as 50 ms in both experiments by considering the persistent time of the fluorescent screen (∼100 ms) in the conventional system. It might be helpful to reduce the effect of afterimage in each acquired pattern compared to shorter exposure times. A camera length of 15 cm was selected for all diffraction patterns.

Data Processing and Orientation Indexing

Orientation indexing of both conventional and CMOS datasets was performed by template matching (Rauch et al., 2010) using the ASTAR software package. Note that all images of the CMOS dataset were binned to 512 × 512 pixels (binning factor of 4) or 128 × 128 pixels (binning factor of 16) and converted to 8-bit depth using a custom-written Python package (Cautaerts, 2020) because the ASTAR software cannot handle the large CMOS dataset nor 16-bit data. The result of this conversion is shown in Supplementary Figure S1. By increasing the binning factor and decreasing bit depth, the diffraction pattern gets more pixelated and the number of gray scale values decreased from 1-65535 to 1-255 (Supplementary Fig. S1). Before template matching was performed, there were default settings for image processing with six different functions (i.e. softening loops, spot enhance loops, spot detection radius, noise threshold, gamma correction, and polar image max work radius). Since artifacts can be induced at some stage, we carefully adjusted these parameters, especially, softening loops, spot enhance loops, and spot detection radius.

The matching index (Q) and reliability (R) of orientation indexing were calculated during the template matching process (Rauch & Dupuy, 2005; Rauch & Véron, 2014). A library of diffraction templates was generated with a lattice parameter of $a = 3.615$ Å for Cu. In the template matching process, experimental patterns are compared to every simulated template that is computed for all possible crystal orientations of all expected phases (Rauch & Dupuy, 2005). The orientation of each experimental pattern is determined to that of the specific simulated template which has the highest matching index. The matching index is determined by a cross-correlation between an experimental pattern and a simulated pattern as given by the following equation.

$$Q = \frac{\sum_{j=1}^{m} P(x_j, y_j) T_i(x_j, y_j, \phi_1)}{\sqrt{\sum_{j=1}^{m} P^2(x_j, y_j)} \sqrt{\sum_{j=1}^{m} T_i^2(x_j, y_j, \phi_1)}} \quad (1)$$

A pattern is represented by the intensity function $P(x, y)$ where x and y are the width and height of the image. For each individual template $T_i(x, y, \phi_1)$ corresponding to a rotation ϕ_1 of the template i taken among the N families stored in the template database

https://doi.org/10.1017/S1431927621012538 Published online by Cambridge University Press

($\phi_1 \in \{1°, 360°\}$, $i \in \{1, N\}$), the summation is performed for every pixel in the pattern image ($j \in \{1, m\}$. Since the simulated pattern has only a limited number of non-zero datapoints (discrete position and intensity of reflections), typically only 50–100 products (i.e. the number of matching reflections) are added during the calculation.

The reliability (R) of orientation indexing is calculated by a ratio of the two highest local maxima after the matching indexes were calculated as given by the following equation.

$$R = 100\left(1 - \frac{Q_2}{Q_1}\right) \quad (2)$$

where Q_1 and Q_2 are the two highest values of the matching indexes for distinct local maxima in all possible orientations.

After orientation indexing, the orientation data were exported (.ang format) and analyzed with the TSL-OIM software (EDAX Inc.). No clean-up process like grain dilation or grain neighboring process was performed to allow direct comparison.

Results

Direct Comparison of Diffraction Patterns Acquired by the Conventional and CMOS Systems

Figure 2 shows a direct comparison of diffraction patterns obtained by using the two different detector setups. Diffraction patterns were acquired near the [110] zone axis of single-crystal Si at the same location of the specimen. In the conventional configuration, the original diffraction pattern is stretched along the vertical axis since the fluorescent screen, where the pattern is acquired using the CCD camera, is inclined with respect to the image plane. After correcting for this inclination, a contraction of the pattern is observed (Fig. 2a). In the CMOS image, more reflections are captured due to the large acceptance angle of the CMOS detector at the same camera length (Fig. 2b). Distortions in the diffraction pattern acquired using the CMOS detector are mainly stemming from astigmatism and aberrations in the objective and projection lens system. The different magnification of the diffraction pattern can be easily adjusted by changing the camera length in diffraction mode.

A quantitative comparison of intensity profiles extracted along 13 systematic row reflections of two representative nanobeam electron diffraction patterns is shown in Figure 2c. Due to the different magnification of pattern images (Figs. 2a, 2b), only eight reflections could be compared (indicated by vertical red lines for the conventional case in Fig. 2c). Note that the intensity of all pixels of the diffraction patterns is amplified with an exponent (~0.5) using a gamma correction of the conventional dataset. This function is normally used to compensate the limited dynamic range and the loss of signal during the data acquisition of the conventional system. This results in a shift of intensity levels from the lower to the middle range of intensities for the conventional dataset (Fig. 2c). Since the effective resolution of the diffraction spots in the conventional setup is largely determined by the point spread function of the phosphor screen, the relative intensities of the transmitted beam and a weak diffracted beam are not remarkable compared to the CMOS detector. In contrast, the pattern acquired by the CMOS detector shows a weak reflection at a high scattering angle (black arrow in Fig. 2c), which is resolved due to the high dynamic range. This result shows the CMOS detector can capture more weak reflections without exposing the camera to a point whereby the transmitted beam is saturated. The radial distribution of the background intensity is observed in both systems, which is mainly dominated by inelastically scattered electrons (Figs. 2a, 2b).

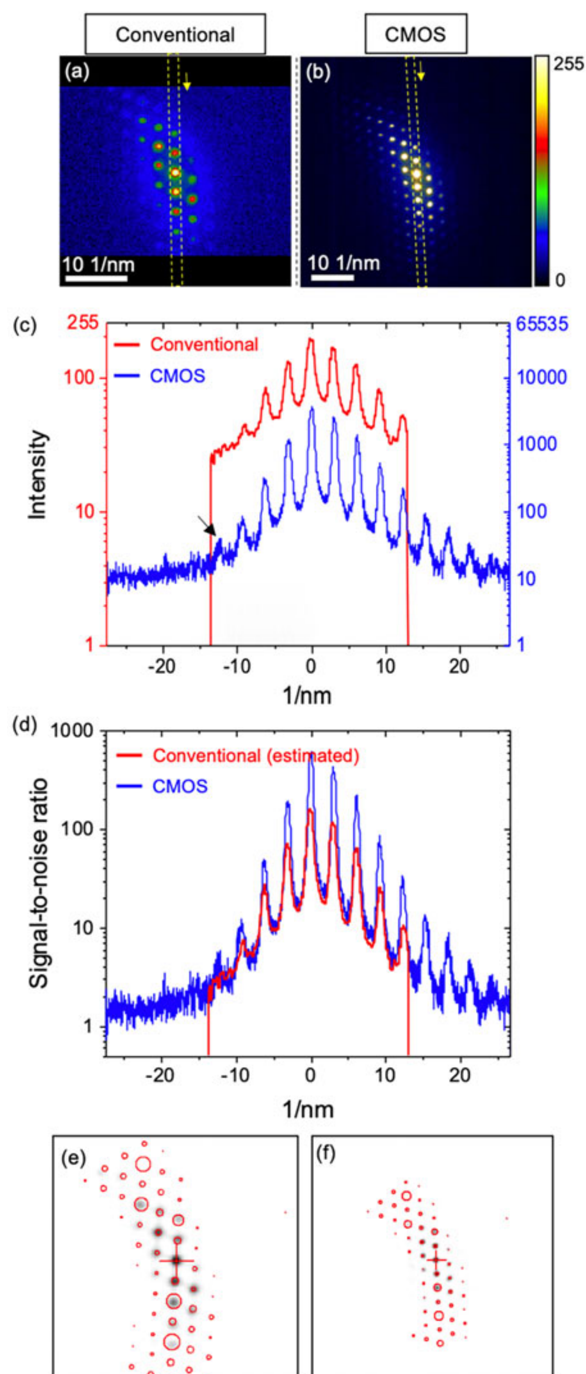

Fig. 2. Direct comparison of diffraction patterns showing near [110] zone axis of single-crystal Si obtained by using conventional and CMOS systems. Raw pattern images with temperature-color scale: (**a**) conventional (144 × 144 pixels) and (**b**) CMOS detector (2k × 2k pixels). Note that pixels with an intensity above 255 are shown as white color. (**c**) Intensity profiles and (**d**) signal-to-noise ratio measured along the same direction in the PED pattern images (marked as yellow square in a and b). Orientation indexing by template matching process for the pattern images obtained by (**e**) conventional and (**f**) CMOS detector. Diffraction spots displayed as red circles represent the simulated pattern with the highest matching index. The size of circles is indicating the relative radius of each reflection in the matched simulated pattern.

https://doi.org/10.1017/S1431927621012538 Published online by Cambridge University Press

Since we used the gamma correction during the acquisition of conventional dataset, the direct comparison of signal-to-noise ratio between two systems is inappropriate because the gamma correction affects the measurement of signal-to-noise ratio. To estimate the signal-to-noise ratio of the conventional system without gamma correction, we calculated the signal-to-noise ratio by using a gamma exponent value of 0.5. The signal-to-noise ratio was calculated as the ratio between the measured intensity and the average intensity of dark noise measured by the conventional (Supplementary Fig. S2) and the CMOS detector (Supplementary Fig. S3). The average intensity of dark noise was measured as 18.96 for the external CCD with a gamma correction in conventional configuration and 6.07 for the CMOS detector (Supplementary Fig. S3b), respectively. The effect of gamma correction on signal-to-noise ratio is shown in Supplementary Figure S4. The signal-to-noise ratio for the CMOS detector is also up to ~5 times higher than that for the conventional system (Fig. 2d). The signal-to-noise ratio of the conventional configuration is degraded by the conversion efficiency of signal from diffracted electron to light on the fluorescent screen and the detection of reflected light through the viewing window with the external CCD camera (Fig. 1) during data acquisition. While there is a significant difference in image quality between the two methods, orientation determination by template matching is usually successful when the pattern image contains many reflections (e.g., zone axis) in both cases (Figs. 2e, 2f).

Direct Comparison of Orientation Maps Acquired by Conventional and CMOS Systems

The orientation maps of the nanocrystalline Cu–Ag alloy acquired by both systems from identical locations of the TEM sample are compared side-by-side in Figure 3. Note that orientation maps are reconstructed by template matching process using similar image resolutions of diffraction patterns [i.e. 144 × 144 pixels for conventional dataset and 128 × 128 pixels (binning factor ×16) for CMOS dataset (Supplementary Fig. S1c)] for fair comparison. The bright-field (BF) image (Fig. 3a) and matching index maps (Figs. 3b, 3c) show nano-sized grains with nanotwins. Σ3 twin boundaries and grain boundaries are represented as yellow (twin), black (high-angle grain boundary, misorientation angle >15°), green (low-angle grain boundary, 5° ~ 15° misorientation angle) on the orientation maps (Figs. 3d, 3e). The BF image (Fig. 3a) and raw orientation maps (Figs. 3b–3e) are broadly in agreement. However, fine details such as small grains (white arrow in Fig. 3e) and nanotwins (yellow arrow in Fig. 3e) can be detected only in the CMOS dataset. Kernel average misorientation (KAM) maps (Figs. 3f, 3g) show local misorientation within each grain to visualize sub-grain boundary (<5° misorientation). The KAM calculates the average misorientation between a pixel and its neighbors, provided that the misorientation does not exceed a predefined threshold value (here 5°). All KAM maps presented in this study were calculated with a fixed kernel to the third neighbors (default value). Sub-grain boundaries are not well shown in both orientation maps due to the limited orientation resolution. However, more artifacts within the grain are observed in the dataset obtained by the conventional configuration (Figs. 3d, 3f). Both methods show a reasonable reliability map (Figs. 3h, 3i) with some dark areas indicating low reliability due to grain overlapping. The orientation resolution is limited to ~1° (the maximum angular difference between adjacent templates is approximately 1° for a library with 1,326 templates) because

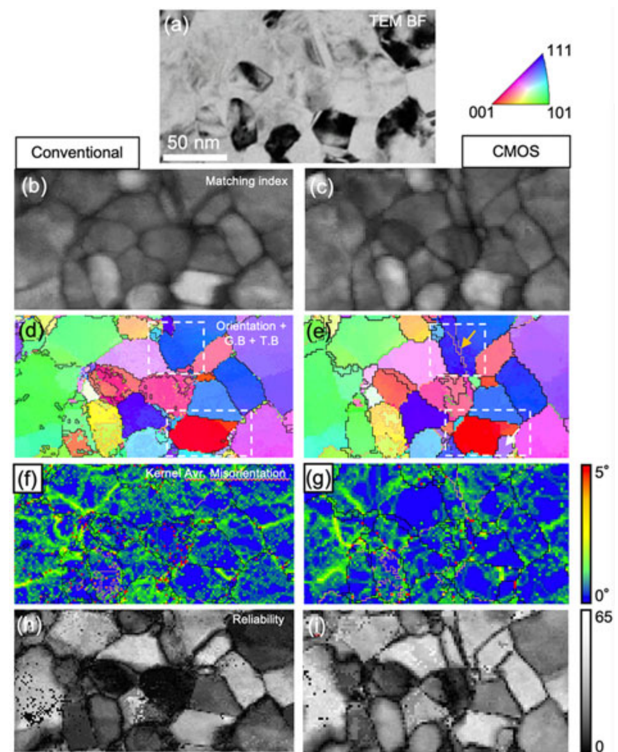

Fig. 3. Side-by-side comparison of orientation maps of nanocrystalline Cu–Ag sample acquired by conventional configuration and CMOS detector. (**a**) BF image, (**b,c**) matching index maps, and (**d,e**) orientation maps. Σ3 twin boundary and grain boundaries are represented as yellow (twin), black (high-angle grain boundary, misorientation angle >15°), green (low-angle grain boundary, 5° ~ 15° misorientation angle). (**f,g**) Kernel average misorientation maps. Sub-grain boundaries (0° ~ 5° misorientation angle) are displayed as a color scale. (**h,i**) reliability maps. The step size was 2 nm for conventional and ~2.7 nm for CMOS. Image resolutions of diffraction patterns were 144 × 144 pixels for conventional dataset and 128 × 128 pixels (binning factor ×16) for CMOS dataset. 1,326 simulated patterns (the maximum angular difference between adjacent templates is approximately 1°) were used for the template matching process.

orientations within 1° of all acquired patterns are only matched by one specific simulated pattern.

A detailed comparison of the grain morphology and corresponding pattern indexing of the conventional and CMOS datasets acquired at the same sample regions are shown in Figures 4 and 5, respectively. Both figures show a BF image of the scanned region, the magnified orientation maps (white dotted square in Figs. 3d, 3e), and corresponding diffraction patterns. In the conventional case, the grain morphology in the orientation map of Figure 4b appears elongated along the scanning direction (i.e. left to right) when compared to the BF image shown in Figure 4a. The diffraction pattern acquired at this grain (marked as a blue circle in Fig. 4b) is matched well with the simulated pattern as shown in Figure 4d. However, when the beam scans the adjacent grain (marked as a yellow circle in Fig. 4b), the afterimage from the previous beam positions is partially present (white dotted circles in Fig. 4e) in the diffraction pattern of the adjacent grain. This effect is prominent in the reliability map because overlapping of afterimage and pattern image decreases the reliability (Fig. 4c). As a result, an incorrect orientation is obtained. This problem is notably observed when the beam is scanning from grains close to zone-axis orientation to grains oriented away from the zone axis or from the sample to vacuum (Viladot

https://doi.org/10.1017/S1431927621012538 Published online by Cambridge University Press

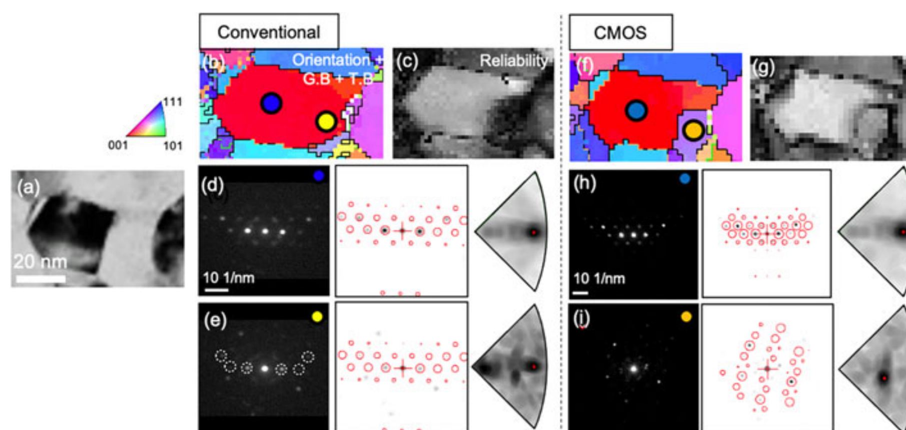

Fig. 4. Comparison of magnified orientation maps showing nano-sized grains acquired by conventional (Fig. 3d) and CMOS detector (Fig. 3e). (**a**) BF image. (**b,f**) magnified orientation maps. (**c,g**) reliability maps. (**d,h**) orientation indexing of the zone-axis oriented grain (marked as a blue circle in **b** and **f**). (**e,i**) orientation indexing of the adjacent grain (marked as a yellow circle in **b** and an orange circle in **f**). Reflections from after image are shown as white dot circles.

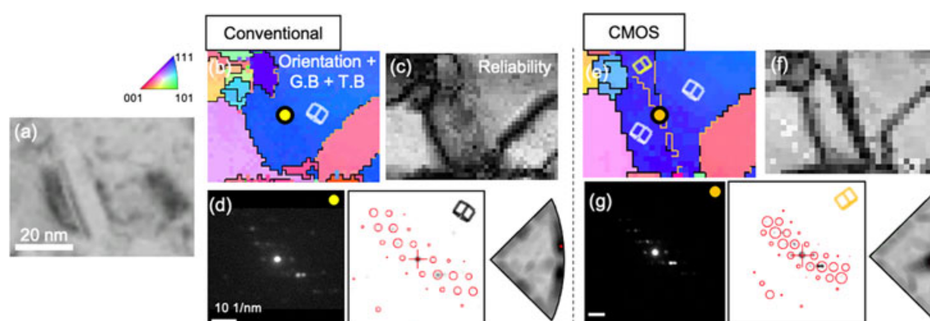

Fig. 5. Comparison of magnified orientation maps showing the grain containing nanotwin acquired by conventional system (Fig. 3d) and CMOS detector (Fig. 3e). (**a**) BF image. (**b,e**) Magnified orientation maps. (**c,f**) Reliability maps. (**d,g**) Orientation indexing of the nanotwin (marked as a yellow circle in **b** and an orange circle in **e**).

et al., 2013). In the present study, the afterimage was observed along the scanning direction with a maximum of 10 pixels (20 nm with a step size of 2 nm), which results in a higher fraction of mis-indexed data points and a decrease in orientation reliability of the orientation map. By considering an exposure time of 50 ms, the persistence time of the afterimage on the fluorescence screen was estimated to be ~500 ms. The decay time might depend on the remaining lifetime of the fluorescent screen. In the CMOS maps, two nearby grains are distinguished (Figs. 4f, 4g) because there is no afterimage present in the diffraction pattern (Figs. 4h, 4i).

Figure 5 shows the orientation mapping analysis for a grain containing a nanotwin with a thickness of ~ 10 nm (Fig. 5a). In the case of conventional data, the nanotwin is not resolved in the orientation map (Fig. 5b) while it is diffusely observed in the reliability map (Fig. 5c). This is because the intensity of reflections in the matrix is amplified due to the afterimage formation in the conventional case as shown in Figure 4. This nanotwin is shown with a thickness of 1~2 pixels in the CMOS orientation map (Fig. 5e). However, the reliability is very low (Fig. 5f) because the diffraction patterns of the matrix and the twin are overlapping with similar intensity (Fig. 5g). Moreover, only a few reflections are visible since the beam direction is away from the zone-axis condition. Due to the advantage of the high dynamic range of the CMOS detector, this nanotwin could be observed by the recognition of a slight difference in the pattern intensity between matrix and twin (Fig. 5g). However, the morphology of the nanotwin is different from that observed in BF image (Fig. 5a). In addition, it is also difficult to verify whether this nanotwin is dominant or not (Fig. 5f).

Orientation Maps Acquired by the CMOS System with Improved Template Matching Process

Although weak reflections were captured by the CMOS detector, the default template matching algorithm cannot utilize weak reflections at high scattering angles. One example is shown in Figure 6. Weak reflections near the detector edge were not matched with the simulated pattern because the reflections near the transmitted beam dominate in the calculation of the matching index. Since they are not orientation sensitive, the template matching is unreliable with ambiguities (Fig. 6c) despite the presence of weak reflections (black arrows in Fig. 6b). In addition, only 1,326 templates could be used for orientation indexing because this problem is more pronounced when a larger number of templates were used (Rauch & Véron, 2014). This makes it difficult to resolve the fine details like sub-grain boundaries because the orientation resolution is limited to 1°.

In order to solve this problem, we excluded reflections near the transmitted beam (dotted circle in Fig. 6d) in the experimental patterns using the fuzzy mask procedure as implemented in the ASTAR software package. The fuzzy mask applies a sigmoidal intensity cutoff of a selected area (here the central beam) in the image of an experimental diffraction pattern. As a result, only

https://doi.org/10.1017/S1431927621012538 Published online by Cambridge University Press

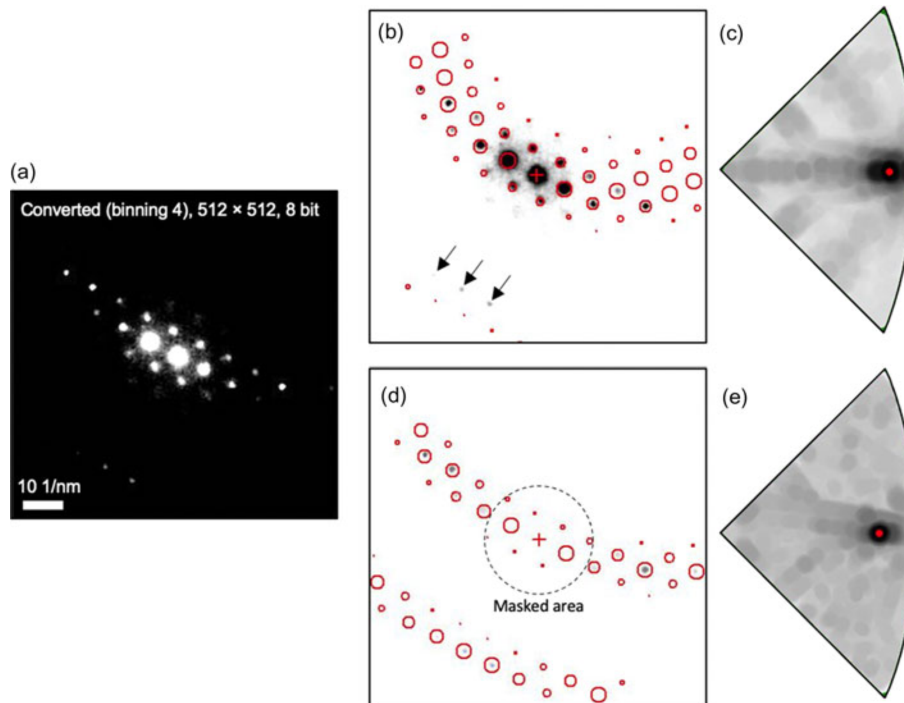

Fig. 6. Orientation indexing by template matching process for (**a**) the pattern image [512 × 512 pixels (binning factor × 4)] acquired by CMOS detector (**b,c**) without masking and (**d,e**) with masking of reflections near transmitted beam (<26 mrad). The masked area is displayed as a black dotted circle. Diffraction spots displayed as red circles represent the simulated pattern with the highest matching index. Orientation is indicated as a red dot in each index map (**c,e**). 11,476 simulated patterns were used for orientation indexing.

weak and small reflections at high scattering angles (>26 mrad) were considered for the template matching process. Even from a visual inspection, a better match of the experimental and simulated patterns is obtained (Fig. 6d). As those reflections are highly orientation sensitive, the reliability of this matching was significantly improved from 8 to 25 with a unique solution (Fig. 6e) while the matching index is decreased from 721 to 305 because the contribution of reflections near the transmitted beam was removed. Note that 11,476 simulated patterns were used for orientation indexing with a maximum angular difference between adjacent templates of approximately 0.33°.

The orientation maps of nanocrystalline Cu-Ag alloy acquired by the CMOS detector using the improved template matching process are shown in Figure 7. Compared to the orientation map reconstructed with conventional template matching (Figs. 3c, 3e), the number of artifacts was significantly reduced (Fig. 7b), especially for the detection of grain boundaries with 2° ∼ 5° misorientation angle. Sub-grain boundaries within the grain are resolved in the KAM map (Fig. 7c). The reliability map (Fig. 7d) contains pixels with low reliability (low value), especially along the grain boundaries. The main reason why the reliability value decreases in the region of the nanotwin is that more than one possible solution from the overlapping patterns exists (Rauch & Véron, 2019). Note that every pixel can show only a single solution (orientation) with the highest value of matching index in the orientation map while two possible solutions are considered when reliability is calculated. In the reliability map, there are some pixels with low reliability inside the grain because the calculation of reliability was incorrect due to the difficulty of finding the two highest local maxima (first and second possible solution for orientation determination) in the matching index map when a large number of simulated patterns were used. Although the calculation of the reliability should be optimized further, these results show that the improved template matching process can significantly enhance the angular resolution of spot patterns when orientation sensitive and weak reflections at high scattering angles are detected in the experimental pattern. The precision and accuracy for the misorientation measurement were estimated using orientations of matrix and twin along the Σ3 twin boundary (white arrow in Fig. 7b) which was not resolved with the conventional case (Fig. 3b). Misorientation angles between matrix and twin were measured along the twin boundaries. Euler angles representing the orientation of the matrix and twin are shown in the supplementary material (Supplementary Table S1). The precision was calculated as the standard deviation of misorientations between matrix and twin. The accuracy was estimated by calculating the difference between ideal misorientation for Σ3 twin (60°) and average measured misorientation between matrix and twin. The angular resolution for misorientation measurement was estimated as 0.20° for precision and 0.27° for accuracy, which is comparable to that of Kikuchi lines (∼0.3°) in TEM (Morawiec et al., 2014).

Discussion

Improving the Template Matching Process & Angular Resolution of the Spot Pattern

In the template matching algorithm (Rauch & Dupuy, 2005), simulated patterns contain only position (not radius) and intensity information of each reflection. The correlation between experimental patterns in the 4D-STEM dataset and the simulated patterns in the template library is performed by calculating the matching index which is the sum of products (i.e. the discrete

https://doi.org/10.1017/S1431927621012538 Published online by Cambridge University Press

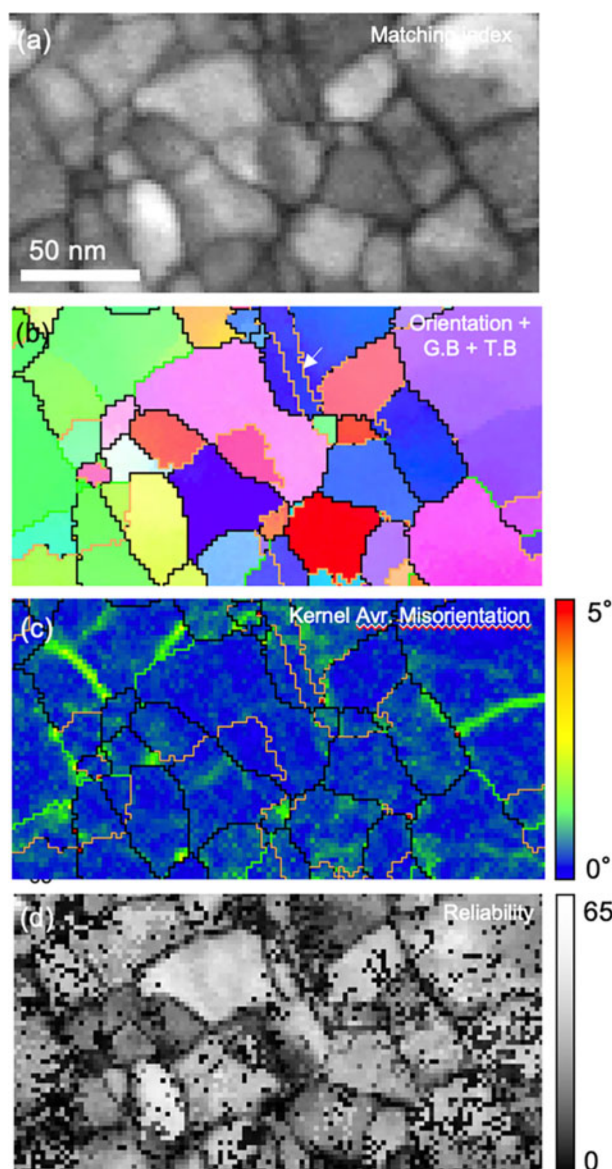

Fig. 7. Orientation maps of nanocrystalline Cu–Ag sample acquired by CMOS detector using improved template matching process (Fig. 6d). (**a**) Matching index map and (**b**) orientation map with Σ3 twin boundary and grain boundaries represented as yellow (twin), black (high-angle grain boundary, misorientation angle >15°), Green (low-angle grain boundary, 5° ∼ 15° misorientation angle), and red lines (grain boundary, 2° ∼ 5° misorientation angle). (**c**) Kernel average misorientation map. Sub-grain boundaries (0° ∼ 5° misorientation angle) are displayed as a color scale. (**d**) Reliability map. Image resolution of diffraction patterns in 4D-STEM dataset was 512 × 512 pixels (binning factor × 4). 11,476 simulated patterns (the maximum angular difference between adjacent templates is approximately 0.33°) were used for the improved template matching process (Fig. 6).

peak intensity values in the simulated pattern times the corresponding measured intensities in the experimental pattern). In simulated patterns, the intensity of reflections at a high scattering angle is relatively high because the atomic scattering factor is not considered (Rauch & Dupuy, 2005) when the pattern was generated, while the intensity of reflections gradually decreases depending on the scattering angle in the experimental pattern (Fig. 2c). This increases the contribution of weak reflections when the matching index is calculated.

However, the current template matching process still could not fully utilize those reflections (Fig. 6b) because orientation indexing is dominated by the high-intensity reflections near the transmitted beam. As these reflections are still close to dynamical diffraction condition under PED and their intensity contains contributions from inelastically scattered electrons, this gives them outsized weight in the calculation of matching index regardless of the contribution of weak reflections. In addition, since they are not orientation sensitive, it can induce mis-indexing of orientation unless the experimental pattern is perfectly corrected in pixels. Therefore, we optimized the template matching process to avoid mis-indexing by applying a fuzzy mask to exclude the reflections near the transmitted beam when the matching index is calculated. As only orientation sensitive and weak reflections are considered, this results in a better agreement between two patterns with an increase of reliability but a decrease in the absolute value of the matching index (Fig. 6).

Orientation mapping with spot patterns in TEM has been shown to have reduced angular resolution compared to Kikuchi-based analysis (Zaefferer, 2011; Morawiec et al., 2014). However, the angular resolution of spot patterns in TEM was not optimized because the conventional data acquisition system has a limited acceptance angle, limited dynamic range, the low resolution of the diffraction images, and low signal-to-noise ratio for detecting weak reflections at high scattering angles. Moreover, although those reflections were captured by the CMOS detector, the current template matching process still has a suboptimal angular resolution. With masked patterns, we could achieve more accurate orientation maps utilizing a large number of templates (high orientation resolution) (Fig. 7).

With the optimization of the acquisition system, number of templates, image resolution of experimental patterns, and image processing, detailed features are getting resolved in the orientation map. One example is the morphology of a nanotwin (Supplementary Fig. S5). The morphology of a nanotwin is gradually changed (Supplementary Figs. S5b, 5c) and finally matched with that of the BF image (Supplementary Fig. S5d). In addition, the reliability of resolving the nanotwin is significantly improved because intensity differences between the matrix and the twin can be clearly distinguished if we consider only reflections at high scattering angles. This indicates that the orientation sensitive, weak, and small diffraction spots at high scattering angles are most significant for orientation mapping.

The Performance of Detectors & Future Remarks

Since orientation mapping is directly affected by the raw image quality of the diffraction pattern, the performance of detectors and data acquisition process are important to obtain high-quality orientation maps. Table 1 shows a comparison between the external CCD camera and recently developed detectors: the scintillator-based CMOS detector and the reverse biased hybrid silicon diode PAD. Note that we only compared detectors which have been used for orientation mapping with SPED. Compared to the conventional case, CMOS and PAD have the advantage of being able to acquire high-quality diffraction images due to increased image resolution and higher dynamic range. Moreover, postprocessing of data is much less affected by artifacts because a distortion correction is not required by on-axis data acquisition unless there is astigmatism in the projector system. However, in the conventional case, mis-indexed data points were observed in the orientation map because the pattern image had a low signal-to-noise ratio with limited digital depth (Figs. 2c, 2d) and suffered from the formation of afterimage

https://doi.org/10.1017/S1431927621012538 Published online by Cambridge University Press

Table 1. Comparison of the Specification of Detectors for PED-Assisted 4D-STEM Data Acquisition at 200 kV.

Sensor Type	Phosphor and CCD (Allied Vision Stingray F-046)	Scintillator-based CMOS (XF416)	Reverse Biased Hybrid Silicon Diode PAD (Merlin)
Mount	External, off-axis	Retractable, on-axis	Retractable, on-axis
Electron sensing mechanism	Phosphor (electron → light) to external CCD (light → signal)	Indirect detection of electrons (electron → light → signal)	Direct detection of electrons (electron → signal)
Detector size (mm^2)	6.47 × 4.81 (1/2″ type)	63.5 × 63.5	28 × 28
Pixel size (μm^2)	8.3 × 8.3	15.5 × 15.5	55 × 55
Image resolution	780 × 580	4,096 × 4,096	256 × 256
Bit Depth (bit)	8–14	16	1–24
MTF (at 200 kV)	–[a]	4% at Nyquist, 27% at Nyquist/2	~10% at Nyquist, ~30% at Nyquist/2
DQE (at 200 kV)	–[a]	~4% at Nyquist, ~28% at Nyquist/2	~10% at Nyquist, ~20% at Nyquist/2
Maximum frame rate (fps)	61 @ 780 × 580 (14-bit), 180 @ 144 × 144 (8-bit)	24 @ 4k × 4k (16-bit), 192 @ 512 × 512 (16-bit)	1,825 (12-bit), 21,000 (1-bit)
Data size (GB, 200 × 200 pixels)	0.85 @ 144 × 144	1,280 @ 4k × 4k, 20 @ 512 × 512	~3.75 @ 256 × 256

Image resolution and dynamic range can be adapted to a purpose (e.g., easy handling of a dataset).
[a]Note that MTF and DQE are not provided for Stingray CCD because this camera is designed for capturing visible light.

(Fig. 4) which could result in incorrect orientation indexing. This might be one reason why a recent study on the comparison between TKD and SPED found a mismatch in the misorientation profiles along the scanning direction beyond stretching or translation that would occur by sample drift (Sugar et al., 2020). The discrepancy between TKD and SPED measurements might be eliminated or reduced if an on-axis electron detector is used.

It is worth comparing the CMOS detector and hybrid silicon diode PAD. While image resolution is less important for orientation and phase indexing, dynamic range, electron sensitivity, and signal-to-noise ratio are crucial parameters. The performance of a detector is quantified by the modulation transfer function (MTF) and detective quantum efficiency (DQE) (Clough et al., 2014). The MTF and DQE are a function of spatial frequency from 0 to 0.5/pixel. The upper limit is known as the Nyquist frequency, which corresponds to a reciprocal of twice the pixel size and is the largest possible frequency obtainable by a pixelated image. In most cases, a PAD shows higher performance because diffracted electrons are directly counted and converted as a signal with a larger pixel pitch ($55 \times 55\ \mu m^2$) in the detector (direct electron detector). The signal is generated in the active layer and then the electrons exit the active layer before significant lateral scattering occurs (Tate et al., 2016). Scintillator-based CMOS systems show a lower performance because diffracted electrons are first converted to photons in the scintillator, and then those are detected by the CMOS after photons have passed through the optical fiber bundle for each pixel pitch ($15.5 \times 15.5\ \mu m^2$) (indirect electron detector). Therefore, a PAD has an advantage to detect diffracted electrons especially under low dose conditions, because it has a higher electron sensitivity based on the fundamentally different sensor structure.

However, when the acceleration voltage is increased to 200 kV, a fall-off in the MTF and DQE is observed in both detectors. This problem is more pronounced in PAD because higher energy electrons spread further sideways in the Si sensor layer than lower-energy ones (Mir et al., 2017*b*; Plotkin-Swing et al., 2020). This means the performance gap between the two detectors closes with increased acceleration voltage. In the case of DQE, the performance of CMOS is comparable to that of PAD at 200 kV although the CMOS detector used in this study exhibits a larger Nyquist limit for a certain camera length (i.e. the image resolution is 4k × 4k for CMOS and 256 × 256 for PAD and the size of the detector is $63.5 \times 63.5\ mm^2$ for CMOS and $28 \times 28\ mm^2$ for PAD) (Table 1). Furthermore, the background intensity induced by inelastically scattered electrons could be reduced by using an in-column energy filter (Ramachandra et al., 2014). In addition, conventional microscopy such as dark-field imaging and diffraction analysis can be performed using the same detector while the previous study required the additional installation of a direct electron detector for a dedicated SPED experiment (Moeck et al., 2011; MacLaren et al., 2020).

Following the significant improvement of orientation analysis shown in the present study, the on-axis CMOS system has further potential to be used for other applications. In practice, the highly binned diffraction patterns are enough to index the orientation (Rouvimov et al., 2009; Rauch et al., 2010; Eggeman et al., 2015). However, if the material consists of multiple phases with similar lattice parameters, using the CMOS detector at full resolution may be useful to provide an even more reliable orientation map, because slight differences in the positions of reflections could be resolved. Following a similar argumentation, in strain measurements, a higher resolution of the diffraction patterns could provide an improved strain resolution. A remaining challenge lies in the analysis of such large datasets, which can exceed 1 TB in size (Spurgeon et al., 2020). Currently, several Python-based packages (de la Peña et al., 2018; Clausen et al., 2019; Savitzky et al., 2019; Duncan et al., 2020) are being developed to process such a large dataset (Paterson et al., 2020), which will lead to improved treatment of the 4D-STEM orientation data and also hold great potential for developing advanced orientation indexing approaches.

Conclusion

We demonstrate a PED-assisted 4D-STEM technique for orientation mapping using spot patterns captured by a fast, scintillator-coupled CMOS detector. While the orientation map obtained by the conventional system shows mis-indexed data points and

https://doi.org/10.1017/S1431927621012538 Published online by Cambridge University Press

scanning noise, the data acquisition with the high-resolution CMOS detector strongly suppresses these artifacts because the image quality of the diffraction patterns was improved by fast read-out rate and high dynamic range of the detector. Moreover, the angular resolution of misorientation measurement could also be improved by optimizing the template matching process with weak reflections at high scattering angle, a large number of templates, and high image resolution of diffraction patterns. Based on the above advantages, fine details such as nano-sized grains, nanotwins, and sub-grain boundaries are resolved in the orientation map.

Supplementary material. To view supplementary material for this article, please visit https://doi.org/10.1017/S1431927621012538

Acknowledgments. This work was supported by the Max Planck Society. The authors thank Dr. Viswanadh Gowtham Arigela for providing Cu–Ag thin foils. G.D. acknowledges financial support by the ERC Advanced Grant GB-Correlate (Grant Agreement: 787446).

References

Bammes BE, Rochat RH, Jakana J, Chen DH & Chiu W (2012). Direct electron detection yields cryo-EM reconstructions at resolutions beyond 3/4 Nyquist frequency. *J Struct Biol* **177**, 589–601.

Cautaerts N (2020). Tvipsconverter 0.1.3. Available at doi: 10.5281/zenodo.4288857.

Clausen A, Weber D, @probonopd, Caron J, Nord M, Müller-Caspary K, Ophus C, Dunin-Borkowski R, Ruzaeva K, Chandra R, Shin J & van Schyndel J (2019). Libertem/libertem: 0.2.2. Available at doi: 10.5281/zenodo.3489385.

Clough RN, Moldovan G & Kirkland AI (2014). Direct detectors for electron microscopy. *J Phys: Conf Ser* **522**, 012046.

Contarato D, Denes P, Doering D, Joseph J & Krieger B (2012). High speed, radiation hard CMOS pixel sensors for transmission electron microscopy. *Phys Procedia* **37**, 1504–1510.

Cooper D, Bernier N & Rouvière JL (2015). Combining 2 nm spatial resolution and 0.02% precision for deformation mapping of semiconductor specimens in a transmission electron microscope by precession electron diffraction. *Nano Lett* **15**, 5289–5294.

de la Peña F, Ostasevicius T, Fauske V, Burdet P, Prestat E, Jokubauskas P, Nord M, Sarahan M, MacArthur K, Johnstone D, Taillon J, Caron J, Migunov V, Furnival T, Eljarrat A, Mazzucco S, Aarholt T, Walls M, Slater T, Winkler F, Martineau B & Donval G (2018). hyperspy: HyperSpy 1.3.1. Available at doi: 10.5281/zenodo.1221347.

Dingley DJ (2006). Orientation imaging microscopy for the transmission electron microscope. *Microchim Acta* **155**, 19–29.

Duncan NJ, Phillip C, Magnus N, Joonatan L, Simon H, Eirik O, Ben M, Carter F, Tina B, Eric P, Stef S, Andrew-ross, Sean C, Ida H, Mohsen, Tom F, Daen J, Niels C, Endre J, Andrew H, Timothy P, Håkon WÅ, Jędrzej M, Phillipcrout, Tiarnan D, Affaniqbal, Tomas O, Mvonlany & Rob T (2020). pyxem/pyxem: pyxem 0.13.0. Available at doi: 10.5281/zenodo.3407316.

Eggeman AS, Krakow R & Midgley PA (2015). Scanning precession electron tomography for three-dimensional nanoscale orientation imaging and crystallographic analysis. *Nat Commun* **6**, 7267.

Ernould C, Beausir B, Fundenberger JJ, Taupin V & Bouzy E (2020). Characterization at high spatial and angular resolutions of deformed nanostructures by on-axis HR-TKD. *Scr Mater* **185**, 30–35.

Fan GY & Ellisman MH (1993). High-sensitivity lens-coupled slow-scan CCD camera for transmission electron microscopy. *Ultramicroscopy* **52**(1), 21–29.

Fundenberger JJ, Morawiec A, Bouzy E & Lecomte JS (2003). Polycrystal orientation maps from TEM. *Ultramicroscopy* **96**, 127–137.

Ganesh KJ, Kawasaki M, Zhou JP & Ferreira PJ (2010). D-STEM: A parallel electron diffraction technique applied to nanomaterials. *Microsc Microanal* **16**, 614–621.

Ghadimi R, Daberkow I, Kofler C, Sparlinek P & Tietz H (2011). Characterization of 16 MegaPixel CMOS detector for TEM by evaluating single events of primary electrons. *Microsc Microanal* **17**, 1208–1209.

Jeong J, Jang W-S, Kim KH, Kostka A, Gu G, Kim Y-M & Oh SH (2021). Crystallographic orientation analysis of nanocrystalline tungsten thin film using TEM precession electron diffraction and SEM transmission Kikuchi diffraction. *Microsc Microanal* **27**, 237–249.

Kobler A & Kübel C (2017). Challenges in quantitative crystallographic characterization of 3D thin films by ACOM-TEM. *Ultramicroscopy* **173**, 84–94.

Li C & Williams DB (2003). Application of automated crystallography for transmission electron microscopy in the study of grain-boundary segregation. *Micron* **34**, 199–209.

Liu J, Lozano-Perez S, Wilkinson AJ & Grovenor CRM (2019). On the depth resolution of transmission Kikuchi diffraction (TKD) analysis. *Ultramicroscopy* **205**, 5–12.

MacLaren I, Frutos-Myro E, McGrouther D, McFadzean S, Weiss JK, Cosart D, Portillo J, Robins A, Nicolopoulos S, Nebot del Busto E & Skogeby R (2020). A comparison of a direct electron detector and a high-speed video camera for a scanning precession electron diffraction phase and orientation mapping. *Microsc Microanal* **26**, 1110–1116.

McMullan G, Faruqi AR & Henderson R (2016). Direct electron detectors. *Methods Enzymol* **579**, 1–17.

Meyers MA, Mishra A & Benson DJ (2006). Mechanical properties of nanocrystalline materials. *Prog Mater Sci* **51**, 427–556.

Mir JA, Clough R, MacInnes R, Gough C, Plackett R, Shipsey I, Sawada H, MacLaren I, Ballabriga R, Maneuski D, O'Shea V, McGrouther D & Kirkland AI (2017*a*). Characterisation of the Medipix3 detector for 60 and 80 keV electrons. *Ultramicroscopy* **182**, 44–53.

Mir JA, Plackett R, Shipsey I & Dos Santos JMF (2017*b*). *Using the Medipix3 detector for direct electron imaging in the range 60 keV to 200 keV in electron microscopy.* arXiv:1710.02227.

Moeck P, Rouvimov S, Rauch EF, Véron M, Kirmse H, Häusler I, Neumann W, Bultreys D, Maniette Y & Nicolopoulos S (2011). High spatial resolution semi-automatic crystallite orientation and phase mapping of nanocrystals in transmission electron microscopes. *Cryst Res Technol* **46**, 589–606.

Morawiec A, Bouzy E, Paul H & Fundenberger JJ (2014). Orientation precision of TEM-based orientation mapping techniques. *Ultramicroscopy* **136**, 107–118.

Nord M, Webster RWH, Paton KA, McVitie S, McGrouther D, MacLaren I & Paterson GW (2020). Fast pixelated detectors in scanning transmission electron microscopy. Part I: Data acquisition, live processing, and storage. *Microsc Microanal* **26**, 653–666.

Oellers T, Arigela VG, Kirchlechner C, Dehm G & Ludwig A (2020). Thin-film microtensile-test structures for high-throughput characterization of mechanical properties. *ACS Comb Sci* **22**, 142–149.

Oleynikov P, Hovmöller S & Zou XD (2007). Precession electron diffraction: Observed and calculated intensities. *Ultramicroscopy* **107**, 523–533.

Ophus C (2019). Four-dimensional scanning transmission electron microscopy (4D-STEM): From scanning nanodiffraction to ptychography and beyond. *Microsc Microanal* **25**, 563–582.

Own CS, Sinkler W & Marks LD (2006). Rapid structure determination of a metal oxide from pseudo-kinematical electron diffraction data. *Ultramicroscopy* **106**, 114–122.

Paterson GW, Webster RWH, Ross A, Paton KA, Macgregor TA, McGrouther D, MacLaren I & Nord M (2020). Fast pixelated detectors in scanning transmission electron microscopy. Part II: Post-acquisition data processing, visualization, and structural characterization. *Microsc Microanal* **26**, 944–963.

Plotkin-Swing B, Corbin GJ, De Carlo S, Dellby N, Hoermann C, Hoffman MV, Lovejoy TC, Meyer CE, Mittelberger A, Pantelic R, Piazza L & Krivanek OL (2020). Hybrid pixel direct detector for electron energy loss spectroscopy. *Ultramicroscopy* **217**, 113067.

Portillo J, Rauch EF, Nicolopoulos S, Gemmi M & Bultreys D (2010). Precession electron diffraction assisted orientation mapping in the transmission electron microscope. *Mater Sci Forum* **644**, 1–7.

Ramachandra R, Bouwer JC, Mackey MR, Bushong E, Peltier ST, Xuong NH & Ellisman MH (2014). Improving signal to noise in labeled biological specimens using energy-filtered TEM of sections with a drift correction strategy and a direct detection device. *Microsc Microanal* **20**, 706–714.

Rauch E, Véron M, Portillo J, Bultreys D, Maniette Y & Nicolopoulos S (2008). Automatic crystal orientation and phase mapping in TEM by precession diffraction. *Microscopy and Analysis* **22**, S5–S8.

https://doi.org/10.1017/S1431927621012538 Published online by Cambridge University Press

Rauch EF & Dupuy L (2005). Rapid spot diffraction patterns identification through template matching. *Arch Metall Mater* **50**, 87–99.

Rauch EF, Portillo J, Nicolopoulos S, Bultreys D, Rouvimov S & Moeck P (2010). Automated nanocrystal orientation and phase mapping in the transmission electron microscope on the basis of precession electron diffraction. *Zeitschrift fur Kristallographie* **225**, 103–109.

Rauch EF & Véron M (2014). Automated crystal orientation and phase mapping in TEM. *Mater Charact* **98**, 1–9.

Rauch EF & Véron M (2019). Methods for orientation and phase identification of nano-sized embedded secondary phase particles by 4D scanning precession electron diffraction. *Acta Crystallogr, Sect B: Struct Sci, Cryst Eng Mater* **75**, 505–511.

Rodriguez JA & Gonen T (2016). High-resolution macromolecular structure determination by MicroED, a cryo-EM method. *Methods Enzymol* **579**, 369–392.

Rouvimov S, Rauch EF, Moeck P & Nicolopoulos S (2009). Automated crystal orientation and phase mapping of iron oxide nano-crystals in a transmission electron microscope. *Microsc Microanal* **15**, 1290–1291.

Savitzky BH, Zeltmann S, Barnard E, lerandc, Brown HG, Henderson M & Ginsburg D (2019). py4dstem/py4DSTEM. Available at doi: 10.5281/zenodo.3333960.

Schwarzer RA (1997). Advances in crystal orientation mapping with the SEM and TEM. *Ultramicroscopy* **67**, 19–24.

Shionoya S & Yen WM (1998). *Phosphor Handbook*. Boca Raton: CRC Press.

Sneddon GC, Trimby PW & Cairney JM (2016). Transmission Kikuchi diffraction in a scanning electron microscope: A review. *Mater Sci Eng R Rep* **110**, 1–12.

Spurgeon SR, Ophus C, Jones L, Petford-Long A, Kalinin SV, Olszta MJ, Dunin-Borkowski RE, Salmon N, Hattar K, Yang WCD, Sharma R, Du Y, Chiaramonti A, Zheng H, Buck EC, Kovarik L, Penn RL, Li D, Zhang X, Murayama M & Taheri ML (2020). Towards data-driven next-generation transmission electron microscopy. *Nat Mater* **20**, 274–279.

Sugar JD, McKeown JT, Banga D & Michael JR (2020). Comparison of orientation mapping in SEM and TEM. *Microsc Microanal* **26**, 630–640.

Tate MW, Purohit P, Chamberlain D, Nguyen KX, Hovden R, Chang CS, Deb P, Turgut E, Heron JT, Schlom DG, Ralph DC, Fuchs GD, Shanks KS, Philipp HT, Muller DA & Gruner SM (2016). High dynamic range pixel array detector for scanning transmission electron microscopy. *Microsc Microanal* **22**, 237–249.

Trimby PW, Cao Y, Chen Z, Han S, Hemker KJ, Lian J, Liao X, Rottmann P, Samudrala S, Sun J, Wang JT, Wheeler J & Cairney JM (2014). Characterizing deformed ultrafine-grained and nanocrystalline materials using transmission Kikuchi diffraction in a scanning electron microscope. *Acta Mater* **62**, 69–80.

Viladot D, Véron M, Gemmi M, Peiró F, Portillo J, Estradé S, Mendoza J, Llorca-Isern N & Nicolopoulos S (2013). Orientation and phase mapping in the transmission electron microscope using precession-assisted diffraction spot recognition: State-of-the-art results. *J Microsc* **252**, 23–34.

Vincent R & Midgley PA (1994). Double conical beam-rocking system for measurement of integrated electron diffraction intensities. *Ultramicroscopy* **53**, 271–282.

Wu G & Zaefferer S (2009). Advances in TEM orientation microscopy by combination of dark-field conical scanning and improved image matching. *Ultramicroscopy* **109**, 1317–1325.

Yang H, Jones L, Ryll H, Simson M, Soltau H, Kondo Y, Sagawa R, Banba H, MacLaren I & Nellist PD (2015). 4D STEM: High efficiency phase contrast imaging using a fast pixelated detector. *J Phys: Conf Ser* **644**, 012032.

Yao X, Amin-Ahmadi B, Li Y, Cao S, Ma X, Zhang XP & Schryvers D (2016). Optimization of automated crystal orientation mapping in a TEM for Ni4Ti3 precipitation in All-round SMA. *Shape Mem Superelasticity* **2**, 286–297.

Zaefferer S (2011). A critical review of orientation microscopy in SEM and TEM. *Cryst Res Technol* **46**, 607–628.

https://doi.org/10.1017/S1431927621012538 Published online by Cambridge University Press